Martensite-enabled magnetic flexibility: The effects of post-growth treatments in magnetic-shape-memory Heusler thin films

Original
Martensite-enabled magnetic flexibility: The effects of post-growth treatments in magnetic-shape-memory Heusler thin films / Takhsha Ghahfarokhi, M., Casoli, F., Fabbrici, S., Nasi, L., Celegato, F., Cabassi, R., Trevisi, G., Bertoni, G., Calestani, D., Tiberto, P., Albertini, F.. - In: ACTA MATERIALIA. - ISSN 1359-6454. - 187:(2020), pp. 135-145. [10.1016/j.actamat.2020.01.049]

Publisher:
Elsevier

Published
DOI:10.1016/j.actamat.2020.01.049

Martensite-enabled magnetic flexibility: The effects of post-growth treatments in magnetic-shape-memory Heusler thin films

Milad Takhsha Ghahfarokhi[a], Francesca Casoli[a], Simone Fabbrici[a], Lucia Nasi[a], Federica Celegato[b], Ricardo Cabassi[a], Giovanna Trevisi[a], Giovanni Bertoni[a], Davide Calestani[a], Paola Tiberto[b], Franca Albertini[a]

a IMEM-CNR, Parco Area delle Scienze 37/A, Parma 43124, Italy
b INRIM, Strada delle Cacce 91, Turin 10135, Italy

Abstract

Magnetic-shape-memory Heusler thin films have a great potential for new-concept integrated devices, such as microactuators, energy harvesters and solid-state microrefrigerators, thanks to the intimate coupling between structure and magnetism. The control of microstructure in their martensitic phase is crucial for their full exploitation. Here, by an accurate magnetic and structural investigation at different length-scales, we demonstrate how growth temperature and simple post-growth treatments, i.e. post-annealing at low T, magnetic field cooling and mechanical stress, are suitable to manipulate the twin variant configuration in epitaxial thin films. X-type variants with out-of-plane magnetic easy axis or Y-type variants with in-plane magnetic easy-axis can be selected, as well as their geometrical distribution in films with mixed X/Y-type microstructure. The mechanisms behind the overall and local manipulation of microstructure are discussed by taking into account the role of microstructural defects, disorder and external fields on the martensitic transformation path. Our findings provide a platform for a controlled manipulation of microstructure and magnetism in magnetic-shape-memory thin films, which opens up a window towards engineering smart magnetic materials for multiple purposes. This remarkable "magnetic flexibility" makes magnetic-shape-memory alloys a unique class, among magnetic materials, for the easy tuning of the magnetic configuration at different length scales.

1. Introduction

Magnetic-shape-memory Heusler materials have the capability of shape recovery through a diffusion-less thermodynamic structural phase transformation (martensitic phase transformation) between high-temperature cubic phase (austenite) and low-temperature lower symmetry phase (martensite). Because of the strong coupling between structural and magnetic degrees of freedom, martensitic transformation can be induced by different external stimuli (i.e., magnetic field, stress and temperature) [1,2]. Thanks to the multifunctional properties linked to the transformation, magnetic-shape-memory materials are prominent candidates for a number of applications, e.g. magnetorefrigerants [3] and energy harvesters [4].

Stoichiometric Ni_2MnGa is a full Heusler compound, which is known as a model system for magnetic-shape-memory materials [5]. Compared to bulk samples, epitaxial films represent a proper system for fundamental investigation due to fine control of microstructure. Additionally, they are promising for being integrated into micro and nanodevices [6,7]. So far, Ni-Mn-Ga epitaxial films have been grown on different types of single crystal substrates such as MgO [8], NaCl, Al_2O_3 [9], GaAs [10], $SrTiO_3$ [11], and YSZ [12].

Across the martensitic transformation, the material encounters coordinated movement of atoms, which produces shear stress in the system. This gives rise to a remarkable change of microstructure: twin variants nucleate and organize in a hierarchical architecture, i.e. interrelated twin-within-twin 3D patterns, to address the compatibility of martensitic and austenitic phases and also of different martensitic variants. The competition between the elastic energy of the system and the twin boundary energy determines the twinning relation, period, length scale and hierarchical growth [13–16]. The martensitic phase often shows a modulated structure [17,18].

Typically, in epitaxial Ni-Mn-Ga films on MgO(100) two different martensitic microstructures, called X-type and Y-type, can form and they may coexist in the same film depending on the substrate or underlayer, composition and growth conditions [19,20 and references therein]. In Y-type microstructure the twin planes grow perpendicular to the substrate surface, while in X-type the twin planes grow at 45° to the substrate surface. The easy-magnetization axis of the martensitic cells lies alternately in-plane and out-of-plane in X-type twin variants, while it alternates between two different in-plane directions in Y-type microstructure [19,21,22]. Controlling twin variants' orientation and their organization in X and Y microstructures is crucial for optimizing the multifunctional properties and could also better enable a number of thermomagnetomechanical applications beyond magnetic refrigeration and energy harvesting, e.g. magnetic domain dependent directional actuation [23,24], magnetic field writing [25,26] and magnetic anisotropy dependent biological applications [27].

So far, there have been few attempts for overall manipulation of microstructure in epitaxial Ni-Mn-Ga films. Jenkins et al. reported the magnetic rearrangement of twin variants in epitaxial Ni-Mn-Ga cantilever released from the substrate [28]. Eichhorn et al. reported partial alignment of twin variants in freestanding epitaxial Ni-Mn-Ga bridges using magnetic field cooling [29]. In 2015, we published a detailed study on the correlation between structure, microstructure and magnetic properties of substrate constrained Ni-Mn-Ga films grown on Cr/MgO(100) and showing the preferential alignment of the Y-type variants along a specific direction [19]. More recently, we reported thermo-magnetic actuation of free-standing Ni-Mn-Ga nanodisks based on the selection of X-type or Y-type twin variants [23].

In addition, there have been some works on local tuning of magnetism both for Ni-Mn-Ga bulk single crystals [25,26] and local reduction of the nucleation barrier in epitaxial films [30].

In this study, we show how to manipulate the microstructure and magnetic configuration of Ni-Mn-Ga films directly grown on MgO (100), changing the twin variants from all X-type to mixed X/Y. We start from films of different morphology obtained by changing growth temperature and apply suitable post-growth treatments, such as post-annealing, magnetic field cooling and a local mechanical stress.

We clearly demonstrate how different simple post-growth treatments open up the possibility to tailor the microstructure of magnetic-shape-memory thin films and consequently obtain the magnetic configuration best suited to the required purpose. This remarkable "magnetic flexibility", enabled by the martensitic micro-structure and the strong spin-lattice coupling of these materials, makes magnetic-shape-memory alloys a unique class among magnetic materials for the easy manipulation of magnetic configuration at different length scales.

2. Experimental section

Ni-Mn-Ga films (200 nm) were grown epitaxially on MgO(100) by rf sputtering. Deposition rate and Ar pressure were fixed at 0.1 $nm \cdot s^{-1}$ and 1.5 Pa, respectively. The effect of growth temperature (T_g) was investigated by growing three different samples at decreasing T_g (from 623 K to 523 K, see Table 1). The compositions of the sputtering target and films were measured by Energy Dispersive X-ray Spectroscopy (EDS), obtaining $Ni_{49.3}Mn_{27.8}Ga_{22.9}$ for the target and Ni-rich, Ga-rich compositions for the films, as reported in Table 1.

Three different types of after-growth treatments were employed: (1) post-annealing of the as-grown samples for 3600 s at 623 K in 10^{-3} mPa (see Table 1 for the names of the post-annealed samples); (2) magnetic field cooling; (3) local stress.

Treatment 2 (magnetic field cooling) was performed on sample #2P The sample was heated up to 338 K in ambient atmosphere and zero magnetic field and cooled down to RT in a magnetic field of 0.5 T applied along the [100] and [010] directions of the MgO crystal (one experiment for each field direction). In each experiment, the sample was characterized after the field-cooling and a further thermal cycle in zero magnetic field (up to 393 K with a heating rate of 0.1 $K \cdot s^{-1}$ and back to RT with a cooling rate of 0.3 $K \cdot s^{-1}$).

Treatment 3 (local stress) was performed on sample #1P A local stress was applied at RT using a stainless steel sharp tool (nominal thickness 228 μm) oriented perpendicular to the substrate surface and crossing the surface along MgO [010] or [110] direction. Unless otherwise noted, the stress was followed by a thermal cycle (up to 393 K with a heating rate of 0.1 $K \cdot s^{-1}$ and back to RT with a cooling rate of 0.3 $K \cdot s^{-1}$).

Magnetic behavior of the samples over temperature was studied by a superconducting quantum interference device (SQUID) magnetometer in the presence of 2 mT in-plane magnetic field along MgO [100].

Temperature-dependent X-Ray Diffraction experiments were performed using a Thermo ARL X'tra diffractometer equipped with a solid-state Si(Li) Peltier detector and an environmental chamber.

Compositional and microstructural measurements were performed using scanning electron microscopy equipped with EDS and BSE modes (SEM, FEI Inspect – F). Different microstructures of twin variant clusters were recognized on BSE image thanks to the electron channeling effect, which provides selective interaction of incident electrons with different crystal orientations [31].

Transmission electron microscopy (TEM) plan view measurements were performed at RT on detached samples prepared by chemical wet etching using TEM (JEOL JEM 2200FS, 200 kV). Locally induced Y-type twin variants were observed by high-angle angular dark field scanning transmission electron microscopy (HAAFD-STEM), high-resolution transmission electron microscopy (HR-TEM) and Fourier transformed electron diffraction patterns (FFT) through cross-section analysis on a lamella prepared by focused ion beam lift-off technique with a Zeiss Auriga Compact Focused Ion Beam system. Electron holography technique was performed on the same TEM apparatus to determine the nanometric magnetic domains of the prepared lamella in cross-section.

Atomic and Magnetic Force Microscopy (AFM, MFM) images were captured using Dimension 3100 microscope equipped with Nanoscope Veeco controller. Magnetic images were taken in interleave mode by MESP-V2 magnetic tips.

Table 1

Growth temperatures, compositions and critical temperatures measured by SQUID magnetometer with a magnetic field of 2 mT along MgO [100] on films with thickness = 200 nm and deposition rate = 0.1 $nm \cdot sec^{-1}$.

Sample (#)	**1**	**2**	**3**	**1P**	**2P**	**3P**
Growth temp. (K)[a]	623	573	523	Sample #1 After annealing	Sample #2 After annealing	Sample #3 After annealing
Ni (at.%)[b]	52.5	52.4	52.0	52.7	52.6	52.3
Mn (at.%)[b]	20.7	20.6	21.8	19.9	20.6	22.9
Ga (at.%)[b]	26.8	27.0	26.2	27.4	26.8	24.8
T_C (K)[c]	340	344	-	338	340	350
T_M (K)[c]	328	326	-	322	317	307
T_A (K)[c]	333	330	-	328	325	311

a Uncertainty ~ 5 K.

b Uncertainty ~ 1 at.%.
c Uncertainty ~ 1 K.

3. Results and discussion

3.1. The effect of growth temperature and post-annealing

The grown films show Ni-rich, Ga-rich compositions (Table 1), differently from the sputtering target ($Ni_{49.3}Mn_{27.8}Ga_{22.9}$), due to the different sputtering yields of Ni, Mn, and Ga [32]. Considering the uncertainty of energy dispersive X-ray spectroscopy (EDS) technique on these samples, the composition does not substantially change neither with growth temperature nor with post-annealing.

Thermomagnetic analysis gives the first clear evidence on how the growth temperature affects the martensitic transformation. The results are reported in Fig. 1a. The film grown at 623 K shows on heating a sharp transition from the ferromagnetic martensitic phase to the ferromagnetic austenitic phase, which soon becomes paramagnetic. This is coherent with our previous results: 623 K was chosen as the optimum growth temperature to obtain the epitaxial austenitic phase at high temperature and a martensitic phase with high structural quality stable at room temperature (RT) [8,19]. The critical temperatures are 328 K for the martensite-austenite transition (T_{MA}) and 340 K for the Curie transition (T_C). The hysteresis of the martensitic transition is around 5 K. When the growth temperature is decreased (samples #2 and #3), the martensitic transition is less and less evident and broadens, while the Curie transition shifts towards high temperature (sample #3). Magnetization, here measured at 2 mT, is also reduced. These characteristics can be due to compositional inhomogeneity, reduced crystalline quality and structural disorder caused by reduced growth temperature.

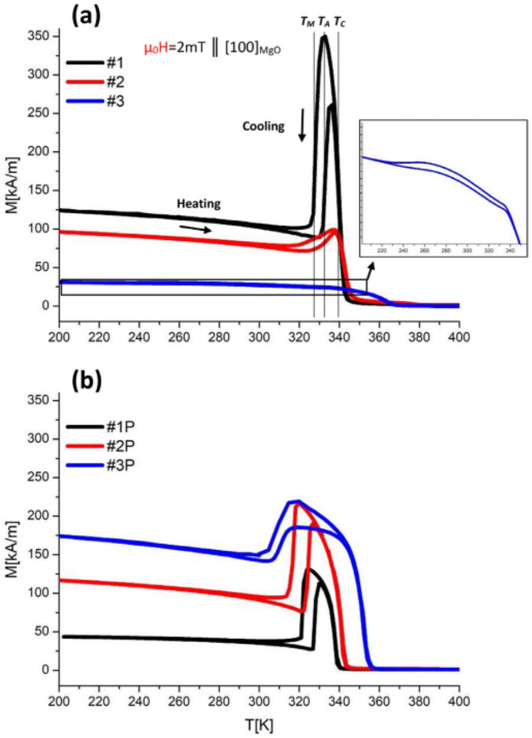

Fig. 1. Magnetic susceptibility over temperature in μH μ_0H = 2 mT along MgO [100] for the as-prepared samples (a) #1, #2, #3 and the corresponding post-annealed samples (b) #1P, #2P, #3P Different samples are represented in different colors (online version). Arrows show the heating and the cooling curves. As an example, the martensitic transformation, austenitic transformation and Curie temperature are labeled for sample #1. Magnified graph of #3 is represented as inset. The critical

temperatures i.e. T_M, T_A and T_C have been measured averaging the start and finish temperatures (uncertainty ~1 K). (For interpretation of the references to colour in this figure legend, the reader is referred to the web version of this article.)

Fig. 1b shows that the post-annealing at 623 K improves the quantity and quality of martensitic phase present in the films grown at lower temperatures, i.e., #2 and #3, increasing the magnetization variation at the martensitic transformation and reducing its broadening. The most evident effect of post-annealing on the film grown at the optimum temperature, i.e. #1, is a small shift of the martensitic transformation towards low temperatures. A higher magnetization was measured for samples #2P and #3P with respect to sample #1P, due to a higher fraction of the film with easy-magnetization direction in the film plane (see below).

The evolution of the structure with temperature was measured using X-ray diffraction (XRD). High temperature XRD for samples #1, #1P, #2, #2P and #3P shows similar epitaxial cubic austenitic structure with (h00) family of crystallographic planes normal to the plane of the film (Fig. 2a). Sample #3, grown at the lowest temperature, shows a different behavior as described further below. As we reduce the temperature, the films encounter martensitic transformation to 7 M monoclinic incommensurate structure [18]. The structural quality, in agreement with the thermo-magnetic analysis, worsens with decreasing the growth temperature. We hereby describe the martensitic structure within the austenitic reference, where the c axis corresponds to the unique axis (and to the easy-magnetization direction) and the modulation direction lies on one of the two a-b plane diagonals. Fig. 2b-g shows 58–70° ϑ–2ϑ scans of the samples in the martensitic state. The figures are parts of wide range (28–70°) scans, which were cut and magnified to improve the legibility. As can be observed, only the (0k0) family of planes of the martensitic cells are detectable by a conventional ϑ–2ϑ scan [8,19]. By tilting the diffraction vector from the substrate normal to approximately 2°, (0k0) planes exit the diffraction condition while (k00) as well as (00k) diffraction peaks appear. This is due to the misorientation of the martensitic cells, i.e., a slight rotation around the b axis to reduce the elastic strain between the two phases [33]. The misorientation is apparent when the b axis is in the plane of the film (X-type). Hence, we can refer the $(040)_M$ to the out of plane b axis in Y-type regions and the $(400)_M$ as well as $(004)_M$ reflections to the X-type regions (for details, readers are referred to ref. [19]). According to this explanation, the relative low intensity of $(040)_M$ in Fig. 2b and c for high temperature grown samples can be attributed to the absence of Y-type twin variants in these two samples. Consistently, if we compare the diffraction patterns of samples #2 (Fig. 2d) and #2P (Fig. 2e) it is possible to appreciate that the $(040)_M$ reflection in sample #2 has a broader profile and a lower relative intensity with respect to the other martensitic $(400)_M$ $(004)_M$ reflections. These features can be justified by the improved crystallinity as well as by the presence of a relatively larger amount of Y-type twin variants in the annealed #2P sample. This was confirmed by Scanning Electron Microscope (SEM) and Magnetic Force Microscope (MFM) measurements (see below). Fig. 2f shows the X-ray analysis for sample #3, which was grown at 523 K. The figure does not show the expected martensitic offset peaks neither at room temperature (RT) nor below RT. Instead, a broad peak is observed in normal scan, which can be attributed to a fundamental $(400)_{bcc}$-like reflection peak originating from a disordered phase where the structural transformation has been hindered. After annealing (sample #3P), the microstructure partially recovers, as testified by the diffraction patterns (Fig. 2g).

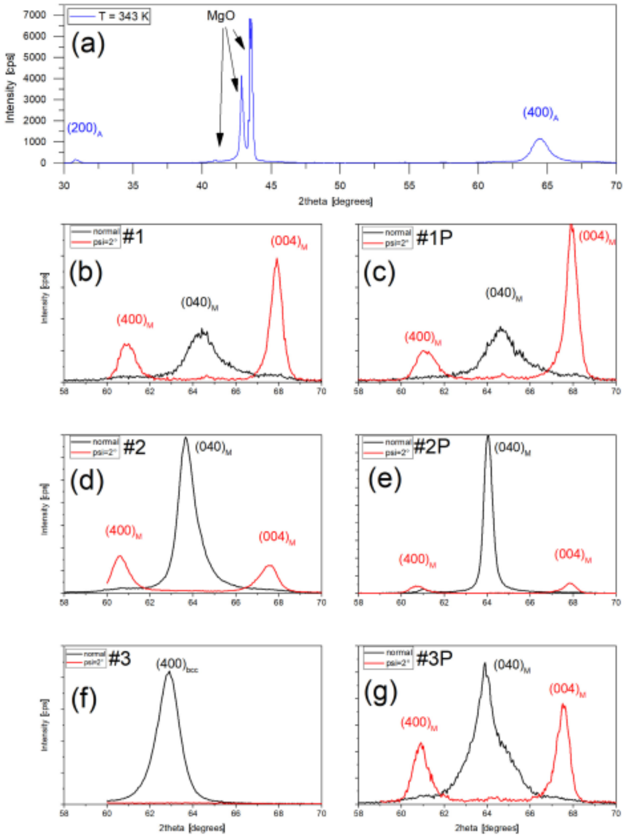

Fig. 2. X-ray diffraction for the as-prepared and post-annealed samples, (a) #1, 2θ = 30–70 at 343 K showing the epitaxial {h00} family of austenite peaks, (b) #1, (c) #1P, (d) #2, ((e) #2P, (f) #3 and (g) #3P, 2θ = 58–70 at 300 K. The term psi = 2° refers to asymmetric theta-2θ scan (2° offset), shown in red color (online version). (For interpretation of the references to colour in this figure legend, the reader is referred to the web version of this article.)

Back-Scattering Electron (BSE) SEM images give an overview of the microstructure, with different contrasts for different crystallographic orientations of twin variants (Fig. 3). Fig. 3a shows large-scale twin variant clusters for sample #1, which are oriented along [110] and [1−10] directions of the MgO substrate, as expected for X-type twins [19]. Dark and bright zones are referred to different twin variants nucleated from different austenitic habit planes [34]. In the as-grown sample the continuity of the twin variant within the clusters is in the range of tens of microns, while after post-annealing (sample #1P) we can notice a much larger coherency of the X-type twin variants, which extends to a few hundreds micrometres (Fig. 3b).

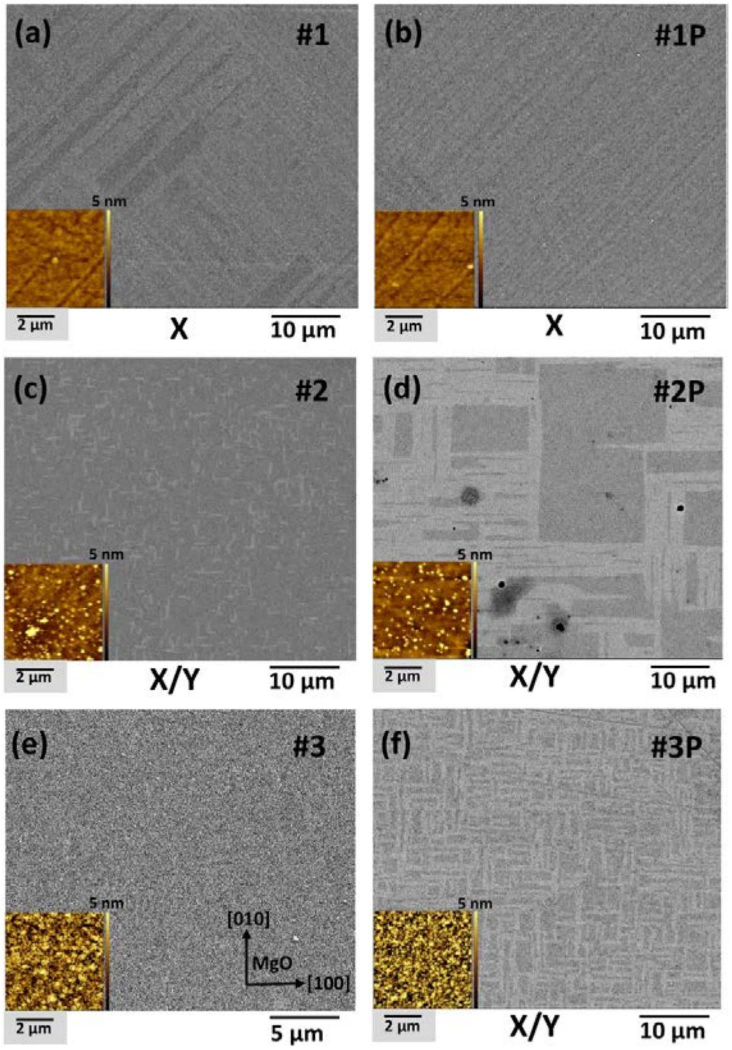

Fig. 3. Large scale BSE images at room temperature showing X-type and Y-type contrasts for the as-prepared and post-annealed samples, insets illustrate the topography images showing the roughness increasing as the growth temperature decreases (a) #1, ((b) #1P, (c) #2, (d) #2P, (e) #3 and (f) #3P The edges of the images are parallel to MgO [100] and [010]. (For interpretation of the references to colour in this figure legend, the reader is referred to the web version of this article.)

Sample #2, which was grown at reduced growth temperature compared to sample #1, shows a striking difference in the BSE image (Fig. 3c). It is the appearance of bright needle-shape contrast zones, oriented along [100] and [010] directions of the MgO substrate in the matrix of dark X-type contrast zones: these are Y-type regions.

In addition, the surface roughness, as measured by atomic force microscopy (AFM, insets in Fig. 3), increases from 0.5 nm to 1.2 nm by reducing growth temperature from T_g = 623 K to 573 K. The post-annealing has a strong effect on the microstructure of the film grown at 573 K (sample #2P, Fig. 3d). Not only the relative length-scale of the twin variants increases compared to the as-grown sample, but also the Y-type twin clusters expand at the expense of X-type zones.

After further reducing the growth temperature to 523 K, we do not see any twin variant contrast in the BSE image (sample #3, Fig. 3e). Surface roughness is also further increased to 2.7 nm. This is in agreement with the X-ray and thermo-magnetic analyses (Figs. 2f and 1a, which evidenced that the dominant structural disorder in sample #3 hinders the martensitic transformation). Despite the absence of twin variants in the as-grown state, after post-annealing the martensitic microstructure is recovered. Fig. 3f in fact shows the contrasts typical of the X and Y zones. Y-type twin variants are dominant and run along the edges of the MgO substrate, though the length-scale of the clusters are lower than in sample #2P

MFM images, captured for the as-grown and annealed samples at RT are reported in Fig. 4a–f. Sample #1 shows the typical out of plane magnetic domain patterns (dark and bright contrasts) of X-type zones. This is due to the perpendicular anisotropy contribution originating from the twin variants with out-of-plane c axis [19]. With decreasing growth temperature, the magnetic domain stripes of sample #1 (Fig. 4a) break down into maze-like patterns with dark/bright contrast of lower intensity (Fig. 4b and c). Areas with no magnetic contrast are also visible. The presence of MFM contrast in sample #3 could be due to the perpendicular anisotropy originating from a strain in the film or from the minority martensitic phase stable at RT (in this sample the transformation is almost completely hindered). The magnetic domain configuration reflects the structure and micro-structure evidenced by XRD and SEM, with a decreased structural quality at low growth temperature and appearance of Y-zones, which are characterized by easy-magnetization c-axes into the film plane.

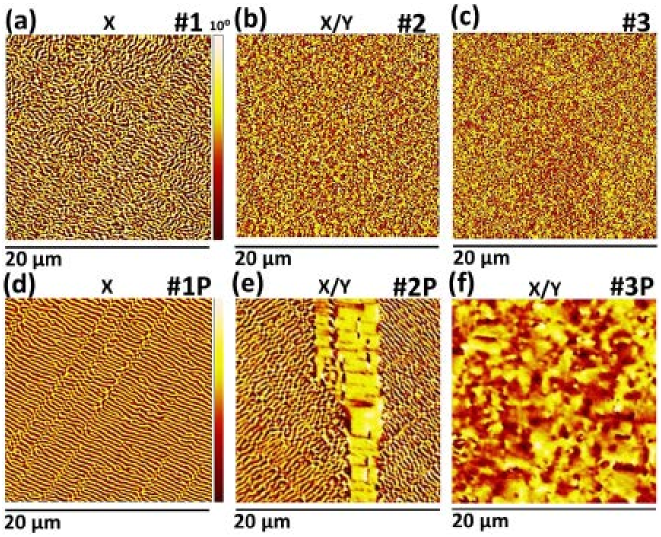

Fig. 4. MFM images at room temperature showing stray field magnetic domain contrast for the as-prepared and post-annealed samples, (a) #1, (b) #2, (c) #3, (d) #1P, (e) #2P and (f) #3P The edges of the images are parallel to MgO [100] and [010]. (For interpretation of the references to colour in this figure legend, the reader is referred to the web version of this article.)

A clear notable modification is observed for the MFM patterns of the annealed samples (Fig. 4d–f). Sample #1P (Fig. 4d) shows very regular stripe domains extending to length-scales of the order of tens of microns, reflecting the coherence of the X-type variants measured by SEM. Sample #2P (Fig. 4e) clearly shows that stripe domain areas (X-type twin variants) are separated by no signal areas. The latter corresponds to Y-type zones, which have in-plane magnetic easyaxis and, as evidenced by the other characterization techniques, are promoted by post-annealing. The coherence of the perpendicular magnetic stripes in the X zones reflects the general improvement of the structure quality after post-annealing. Finally, Fig. 4f shows isolated areas containing a mixture of out-of-plane and in-plane magnetic domains, which are quite larger than the domain islands in #3, and correspond to the X/Y microstructure evidenced by SEM (Fig. 3f).

Transmission electron microscopy (TEM) was performed on samples #1 and #2 to study the hierarchical architecture of the structures from micro-to-atomic scale.

Scanning Transmission Electron Microscopy (STEM) image in Fig. 5a shows a High-Angle Annular Dark-Field (HAADF) plan view of X-type twin variants in #1. Since thickness and elemental composition are constant throughout the specimen, the contrasts in the HAADF image can be ascribed to diffraction contrast due to different crystallographic orientations of twin variants or to martensitic structural modulation.

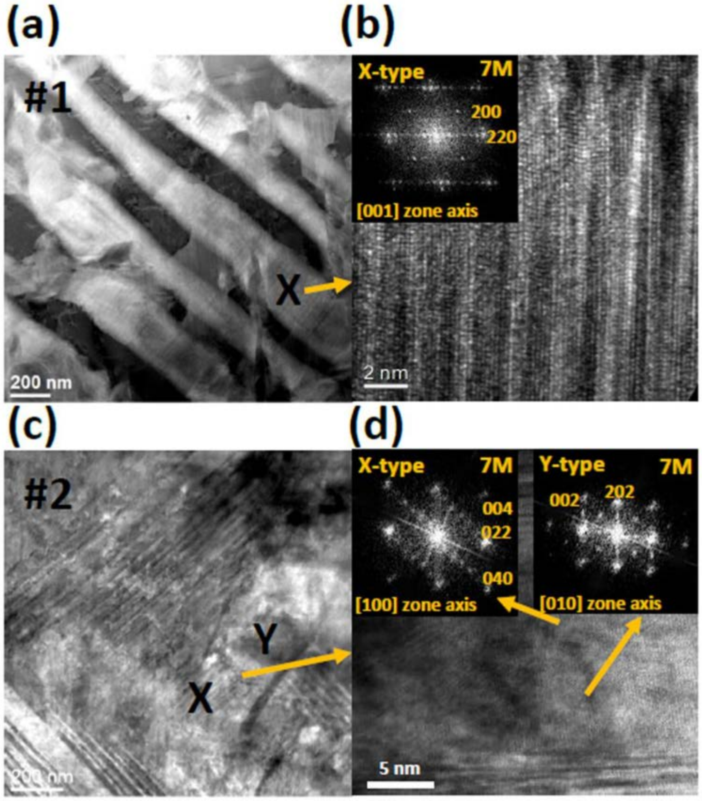

Fig. 5. TEM analysis for samples #1 and #2. Sample #1: (a) HAADF-STEM, (b) HRTEM taken in the zone marked by the arrow in panel a) and the corresponding FFT. Sample #2: (c) HAADF-STEM image, (d) HRTEM of X- and Y-type adjacent regions taken in the zone marked by the arrow in panel c) and related FFTs. The edges of the images are parallel to MgO [100] and [010].

Stripe contrast pattern is observed, with stripes along the [110] and [−110] directions of MgO substrate and stripe width in the range from a few hundreds of nanometres to approximately 20 nm. This contrast is associated with twin variants with different crystallographic orientations.

Martensitic fine contrast modulation parallel to the [100] and [010] directions of MgO is also visibly observed in the regions where the modulation vector lies in the plane of the film, meaning that the easy-magnetization direction is oriented along the out-of-plane direction. Fig. 5b shows a typical high-resolution transmission electron microscopy (HRTEM) image. The associated Fast Fourier Transform (FFT) in the inset clearly shows the satellite spots typical of 7 M modulated structure with the modulation vector perpendicular to the observation direction.

The HAADF and HRTEM analyses confirmed the co-existence of X- and Y-type twin variants in sample #2. The HAADF image in Fig. 5c shows both stripe contrast patterns oriented at 45° and 90° with respect to the substrate edges. A HRTEM image in a region containing both the X and Y variants is shown in Fig. 5d. The FFTs taken in two adjacent regions present the typical pattern of X- and Y-type variants. It is worth noting that, differently from the pattern shown in Fig. 5b, the X-type variant observed here has the magnetization vector in-plane, i.e., the modulation vector inclined to the film plane.

In this class of materials the martensitic transformation occurs into two steps, starting with nucleation of phase boundaries, where the austenitic and martensitic phases are connected and proceeding with the growth of one phase at the expense of the other. Any approach, which reduces the lattice misfit or volume change between the two phases, decreases the energy barrier of the transformation. In the transformation the defects play the role of nucleation points, since the energy barrier is considerably reduced close to imperfections due to the local elastic field [30,35]. This has been exploited to facilitate structural transformation and reduce the hysteresis in magnetocaloric and shape-memory compounds by using ion irradiation or growing precipitates [36,37].

In our films, by reducing growth temperature from sample #1 to #3, the diffusion energy of Ni, Mn, and Ga atoms reduces, therefore atoms with lower energy form nanometric inclusions and inhomogeneities, as also observed by Sharma et al. for thicker films [38]. Consequently, the roughness of the films increases by a factor of six from #1 to #3. These inclusions in sample #2 play the role of nucleation points by applying a large number of local elastic fields to the film. As the martensitic phase nucleates from a large number of points, the length scale of twin variant clusters decreases compared to sample #1. As for sample #3, besides inclusions and microstructural defects, atomic disorder plays a primary role in inhibiting the martensitic transformation. After annealing, defects and imperfections reduce [39] and ordering occurs due to heat diffusion along both the surface and volume of the films, therefore the nucleation sites decrease and martensite growth increases, which enlarges the length scale of twin variant clusters (#1P, #2P). For sample #3P, partial recovery of the structure through annealing promotes the transformation, though the length scale of twin variants is the lowest (compared to #1P and #2P). It was also observed that the samples grown at lower temperature select mixture of X-type and Y-type microstructures. Since the other effective variables (thickness and sub-strate) are not varied, we suggest that in samples #2, #2P and #3P Y-type orientation of twin variants is energetically favoured close to the local elastic field of the imperfections. Previous literature has already pointed out that Y-type twins have been found to nucleate first at the initial stages of martensitic transformation [21,30]. Sample #3P has the largest number of nucleation sites and consequently the largest fraction of Y-type twin variants.

In summary, decreasing growth temperature introduces defects and disorder in the austenic phase and changes the martensitic transformation path by giving rise to different microstructures, from full X-type to mixed X/Y-type. Instead, post-annealing reduces the defects and alters the transformation route.

Taking advantage of both effects, one can tailor the variant configuration: from full X-type to mixed X/Y-type with controlled patterns.

3.2. The effect of magnetic field cooling

We selected sample #2P (characterized by X- and Y-type mixed microstructure) for investigating the possibility to control twin variants' microstructure through in-plane magnetic field cooling, due to the presence of both the types of twin variants in this film, which are pronounced and detectable by AFM/MFM technique.

We applied the magnetic field along MgO [100] and [010] directions and performed the MFM measurements ex-situ at RT on an area of approximately 2500 µm². Results are shown in Fig. 6. The MFM image of the as-grown sample (Fig. 6a) shows the areas corresponding to the two types of twinned microstructure. The major area (approximately 84% of the whole scanned area) corresponds to X-type variants, with the twin boundaries along MgO [1−10] direction (inclined white lines). Y-type zones are evident in the right side portion of the image, which are oriented along [010] direction of MgO and correspond to ~4% of the surface, and at the bottom, which are oriented along MgO [100] direction and occupy 12% of the scanned area (horizontal white lines). The as-grown sample was heated up to 338 K and cooled down to RT in the presence of a 0.5 T field along MgO [010], as sketched in the figure. The experiment was followed by a thermal cycle (up to 393 K and back to RT in $\mu_0H = 0$) in order to measure in the demagnetized state. The resulting MFM image (Fig. 6b) evidences the propagation of Y-type zones at the expense of X-type zones, along both MgO [100] and [010]. This modification is stable after further thermal cycling, possibly due to the advantage in magnetostatic energy of Y-type microstructure compared to X-type microstructure, while the latter is favoured by the epitaxial constraint. A coherent and complete interpretation of this experimental evidence would require a theoretical modeling able to take into account the complexity of this system in terms of elastic and magnetic terms and of their temperature evolution across the transformation.

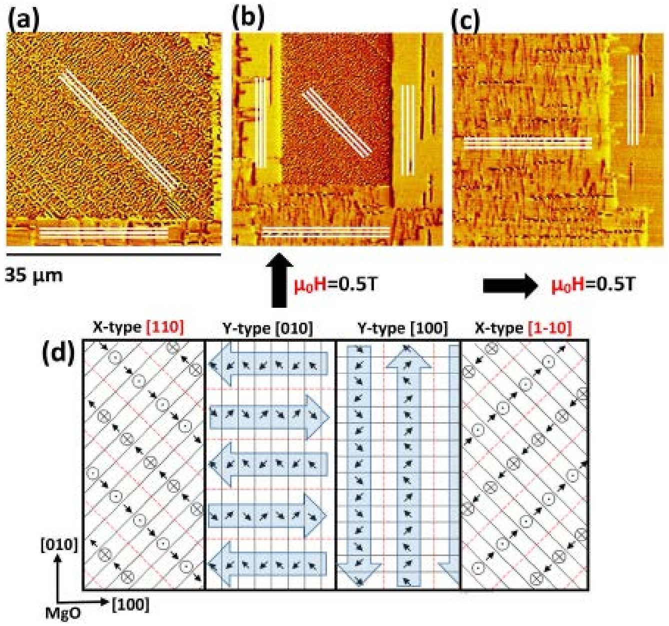

Fig. 6. MFM images at room temperature showing the overall manipulation of twin variants by changing X-type into Y-type through magnetic field cooling of sample #2P The evolution of twin variants can be followed through the white lines, (a) starting sample, (b) cooled from 338 K in the presence of in-plane magnetic field μ_0H = 0.5 T along MgO [010] followed by cooling from 393 K in μ_0H = 0, (c) cooled from 338 K in the presence of in-plane magnetic field μ_0H = 0.5 T along MgO [100] followed by cooling from 393 K in μ_0H = 0, (d) schematic representation of magnetic domains and twin boundaries in X- and Y-type, directions of black arrows show the easy magnetization direction, black lines represent twin boundaries, dash lines show 180° magnetic domain walls and the superimposed light blue arrows illustrate the directions of resultant magnetic vectors in Y-type twin boundaries. (For interpretation of the references to colour in this figure legend, the reader is referred to the web version of this article.)

Comparing Fig. 6a and b, we could estimate that the surface area occupied by X-type variants was reduced from ~84% to ~38% and conclude that the majority of Y-type twin variants after in-field cooling was oriented along the direction of the applied magnetic field, i.e., [010] direction of MgO. This was calculated as $(S_{Y[010]} \cdot S^{-1}_{Y[tot]}) \times 100 \simeq 58\%$, where $S_{Y[010]}$ corresponds to the surface area occupied by Y-type twin variants along the [010] direction and $S_{Y[tot]}$ to the total surface area occupied by Y-type twin variants. The experiment was followed by another field-cooling step (applying 0.5 T along [100] direction of MgO), followed by a thermal cycle (up to 393 K and back to RT in μ_0H = 0). As observed in Fig. 6c, after this further field cooling almost the whole surface area shows Y-type twin variants; approximately 78% of the total surface area was occupied by Y-type twin variants aligned along the direction of the applied magnetic field ([100] direction of MgO substrate).

The experiments described above demonstrate how the twin microstructure of magnetic-shape-memory thin films can be modified by applying an external magnetic field while crossing the martensitic transition on cooling. Thanks to the additional Zeeman energy term and the strong spin-lattice coupling, the twin variants with easy-magnetization direction parallel to the applied field are energetically favoured and grow at the expense of the competing twin variants' type [19,22]. In Fig. 6, the field was applied in the plane of MgO substrate therefore the nucleation of Y-type twins is energetically favoured (easy-axis in plane). The direction of twin boundaries and magnetic domains in X- and Y-type areas are sketched in Fig. 6d, as we previously deduced by electron holography and MFM analyses [19]. The figure also illustrates the overall direction of magnetization in adjacent magnetic domains in Y-type regions (light blue arrows).

In summary, even if the equivalent compressive stress of the applied magnetic field is of moderate intensity (two order of magnitude lower than the typical residual stress reported for epitaxial Ni-Mn-Ga thin films grown on MgO), its application during the temperature induced martensitic transformation is effective in changing the micro-structural patterns. The present experiments definitely show that for Ni-Mn-Ga films with X- and Y-type mixed microstructure, the martensitic transformation path is very sensitive to small variations in the boundary conditions and can be easily influenced. A prevalent Y-type microstructure can be obtained for in-plane applied magnetic fields.

3.3. The effect of local stress

We selected sample #1P, which shows only X-type twin variants, for investigating the possibility to induce Y-type variants by applying a local mechanical stress to the sample. A stress normal to the film along MgO [010] substrate surface was applied to the sample, as described in the experimental section; the stress application was followed by a thermal cycle across the martensitic transition (up to 393 K and back to RT).

A sketch of the microstructure for the stressed sample has been reported in Fig. 7a and b, showing a number of stripes along MgO [010]. The length of the stripes was measured as tens of microns, the width in the range 0.4-2 µm, while the height in the range 4-50 nm. The MFM and its corresponding topography height-section image (Fig. 7c and d) measured at RT show stripe-like Y-type micro-structures appearing along MgO [010] direction.

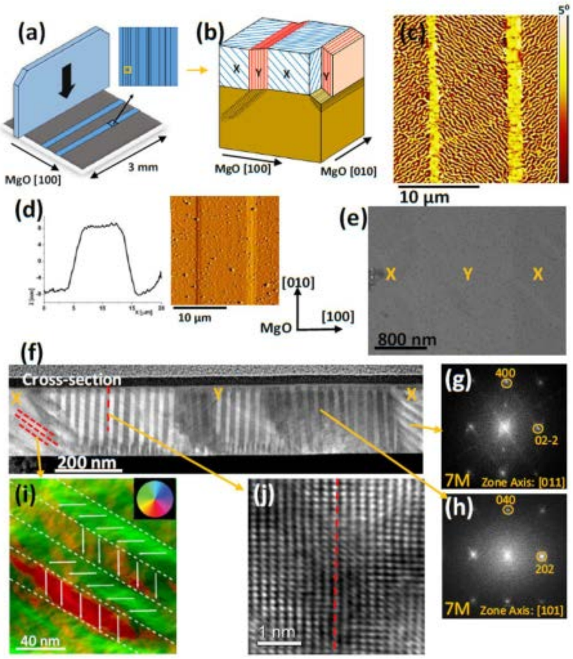

Fig. 7. Local control of microstructure by mechanical stress for sample #1P: (a) schematic representation of the applied stress along [010] MgO and the corresponding arrays of dislocations for 3 × 3 mm sample, (b) 3D representation of the region in the yellow box showing the dislocated arrays of planes in MgO and the related Ni-Mn-Ga microstructure on top, (c) MFM image of the stressed area at RT and d) its corresponding topography and the height section, (e) plan view SEM image of the stress area, (f) cross-section HAADF-STEM analysis of twin variants and (g and h) corresponding FFT analysis pointed by arrows, (i) magnetic induction color map obtained by electron holography for X-type region in cross-section, colors represent the

magnetization directions and color saturation indicates the magnetization intensity; (j) HRTEM image of the marked twin boundary in Y-type. (For interpretation of the references to colour in this figure legend, the reader is referred to the web version of this article.)

The stressed sample was further investigated by several TEM techniques including electron holography. The induced Y-type region shown in the SEM image in Fig. 7e was investigated by cross-section TEM analysis. This confirmed the induced Y-type twin variants. Typical Y-type lamellae perpendicular to the interface are shown in the HAADF image of Fig. 7f. The HRTEM images with corresponding FFTs taken in- and out of the stress-induced area clearly demonstrate that the c axis is out of the plane for the observed X-type region (Fig. 7g) while b axis is out of plane in Y-type region (Fig. 7h). No detachment of the film from the substrate was observed.

The correlation between the twin structure and the magnetic configuration has been directly visualized by means of in-line electron holography experiments that provide the direct evidence of the magnetic patterns inside the twinned regions. Fig. 7i shows the magnetic induction color map obtained by electron holography in X-type region. The direction of the easy-magnetization axis pointing alternatively out-of-plane and in-plane at each lamella is indicated by arrows. The cross-section geometry does not allow to visualize the magnetic contrast from Y-type lamellae being the easy-magnetization axis always in plane.

We also determined the twinning relation of different variants in the stressed region. As can be observed through the HRTEM image (Fig. 7j), the continuity of the atomic planes does not change across the twin boundary, therefore, the twin boundary can be described as type-II [19]. In attempting to understand the mechanism generating the Y-type stripes after stress application, we investigated the surface deformation around the regions subjected to mechanical stress for both the film and an MgO reference substrate. We also altered the direction of the stress from MgO [010] to MgO [110]. The results are shown in the supplementary material. SEM-BSE and AFM analyses of the stressed regions (Figure S2 to Figure S4) show the typical arrays of dislocations along MgO [010], as observed in stress-treated MgO substrates. The applied stress values (not directly measured in our experiment) were estimated to be >20 MPa, by comparing our topographic results on MgO reference substrate with the experimental and simulated results reported in [40,41].

As reported for micro-indentation tests in (001) MgO surface [39,40], the dislocations along the [100] and (or) [010] directions correspond to slip lines dislocations emerging at the free surface, which are visible in topography as they produce emerging deformations perpendicular to the surface.

The two possible martensitic configurations (X- and Y-type) for epitaxial Ni-Mn-Ga films on MgO [100] have a precise geometry with respect to the substrate. Since the direction of slip lines on the film surface (i.e. MgO [010]) matches the orientation of Y-type twin boundaries, the nucleation of Y-type microstructure in the stressed regions is geometrically favoured. This interpretation is supported by a model proposed for the formation of the martensitic hierarchical microstructure of Ni-Mn-Ga epitaxial thin films, based on the well oriented creation and oriented growth of twinned martensitic nuclei [21]. The in-plane and spatial orientation of the nuclei of the two different microstructure (X- and Y-type) is different. In the case of Y-type microstructure, the diamond-like nuclei have high aspect ratio between the two axes, and the long axis is aligned along MgO [010]. A simplified cross-section sketch is reported in Figure S2b, showing the possible relation between the dislocations and Y-type lamellae.

It was also found that the height and slope of the slip lines are important factors for the local inducement of Y-type microstructure (Figure S4). The X-type microstructure remains unchanged up to ~4 nm surface relief (slope ≅ 0.5°), while for the slip lines up to ~23 nm (slope ≅ 2.0°) Y-type appears only after thermal cycle and, for higher values, X-type converts to Y-type at RT.

In summary, we have demonstrated that the application of stress after growth locally transforms X-type twin variants into Y-type along selected direction of substrate. These findings, represents a first step towards the easy manipulation of microstructural and magnetic patterns in magnetic shape memory thin films by the application of local stress after growth.

4. Conclusion

In conclusion, we have shown how different simple post-growth treatments (i.e. post-annealing, magnetic field cooling and the application of a local mechanical stress) open up the possibility to tailor the microstructure of magnetic-shape-memory epitaxial thin films.

Taking advantage of growth temperature and post annealing treatment, microstructure can be easily tuned from full X-type to mixed X/Y-type with different geometrical distribution, by controlling defects and disorder affecting the martensitic transformation path.

Mixed X/Y-type microstructure can be modified by applying an external magnetic field while crossing the martensitic transformation, exploiting the additional Zeeman energy term. In this case, with the field applied in the film plane, a predominant Y-type microstructure can be obtained.

The application of stress after growth is suitable for locally transforming X-type to Y-type twin variants along the direction of stress application.

These results clearly demonstrate the ultimately controllable and flexible microstructure of magnetic-shape-memory films, which is a key point for developing new concept thermo-magneto-mechanical devices. The microstructural and micromagnetic configuration best suited to an application purpose can be now obtained after growth, by locally applying suitable external fields.

In addition, the remarkable “magnetic flexibility”, enabled by the martensitic microstructure and the strong spin-lattice coupling, makes magnetic-shape-memory alloys a unique class among magnetic materials, for the easy manipulation of magnetic configuration at different length scales.

References

[1] K. Ullakko, J.K. Huang, C. Kantner, R.C. O’Handley, V.V. Kokorin, Large magnetic-field-induced strains in Ni_2MnGa single crystals, Appl. Phys. Lett. 69 (1996) 1966-1668.

[2] R.C. O’Handley, Model for strain and magnetization in magnetic shape-memory alloys, J. Appl. Phys. 83 (1998) 3263–3270.

[3] T. Gottschall, A. Gràcia-Condal, M. Fries, A. Taubel, L. Pfeuffer, L. Mañosa, A. Planes, K.P. Skokov, O. Gutfleisch, A multicaloric cooling cycle that exploits thermal hysteresis, Nat. Mater. 17 (2018) 929–934.

[4] M. Kohl, M. Gueltig, F. Wendler, Coupled simulation of thermo-magnetic energy generation based on Ni-Mn-Ga heusler alloy films, Shape Mem. Superelasticity 4 (2018) 242–255.

[5] I. Galanakis, Theory of Heusler and Full-Heusler Compounds, Springer, Cham, UK, 2016.

[6] D.C. Dunand, P. Müllner, Size effects on magnetic actuation in Ni-Mn-Ga shape-memory alloys, Adv. Mater. 23 (2011) 216–232.

[7] A. Backen, S.R. Yeduru, A. Diestel, L. Schultz, M. Kohl, S. Fähler, Epitaxial Ni-Mn-Ga films for magnetic shape memory alloy microactuators, Adv. Eng. Mater. 14 (2012) 696–709.

[8] P. Ranzieri, S. Fabbrici, L. Nasi, L. Righi, F. Casoli, V.A. Chernenko, E. Villa, F. Albertini, Epitaxial Ni-Mn-Ga/MgO (1 0 0) thin films ranging in thickness from 10 to 100 nm, Acta Mater. 61 (2013) 263–272.

[9] T. Eichhorn, G. Jakob, Structural and magnetic properties of epitaxial Ni_2MnGa thin films, Mater. Sci. Forum 635 (2010) 155–160.

[10] J.W. Dong, L.C. Chen, C.J. Palmstrøm, R.D. James, S. McKernan, Molecular beam epitaxy growth of ferromagnetic single crystal (001) on (001) GaAs, Appl. Phys. Lett. 75 (1999) 1443–1445.

[11] O. Heczko, M. Thomas, J. Buschbeck, L. Schultz, S. Fähler, Epitaxial Ni-Mn-Ga films deposited on and evidence of magnetically induced reorientation of martensitic variants at room temperature, Appl. Phys. Lett. 92 (2008) 072502.

[12] Y. Zhang, R.A. Hughes, J.F. Britten, W. Gong, J.S. Preston, G.A. Botton, M. Niewczas, Epitaxial Ni-Mn-Ga films derived through high temperature in situ depositions, Smart Mater. Struct. 18 (2009) 025019.

[13] P. Müllner, A.H. King, Deformation of hierarchically twinned martensite, Acta Mater. 58 (2010) 5242–5261.

[14] A. Saxena, Y. Wu, T. Lookman, S.R. Shenoy, A.R. Bishop, Hierarchical pattern formation in elastic materials, Phys. A 239 (1997) 18–34.

[15] L. Sun, X. He, J. Lu, Nanotwinned and hierarchical nanotwinned metals: a review of experimental, computational and theoretical efforts, npj Comput. Mater. 4 (2018) 1–14.

[16] L. Zhou, M.M. Schneider, A. Giri, K. Cho, Y. Sohn, Microstructural and crystallographic characteristics of modulated martensite, non-modulated martensite, and pre-martensitic tweed austenite in Ni-Mn-Ga alloys, Acta Mater. 134 (2017) 93–103.

[17] L. Righi, F. Albertini, E. Villa, A. Paoluzi, G. Calestani, V. Chernenko, S. Besseghini, C. Ritter, F. Passaretti, Crystal structure of 7 M modulated Ni-Mn-Ga martensitic phase, Acta Mater. 56 (2008) 4529–4535.

[18] L. Righi, F. Albertini, S. Fabbrici, A. Paoluzi, Crystal structures of modulated martensitic phases of FSM Heusler alloys, Mater. Sci. Forum 684 (2011) 105–116.

[19] P. Ranzieri, M. Campanini, S. Fabbrici, L. Nasi, F. Casoli, R. Cabassi, E. Buffagni, V. Grillo, C. Magén, F. Celegato, G. Barrera, P. Tiberto, F. Albertini, Achieving giant magnetically induced reorientation of martensitic variants in magnetic shape-memory Ni-Mn-Ga films by microstructure engineering, Adv. Mater. 27 (2015) 4760–4766.

[20] J. Tillier, D. Bourgault, P. Odier, L. Ortega, S. Pairis, O. Fruchart, N. Caillault, L. Carbone, Tuning macro-twinned domain sizes and the b-variants content of the adaptive 14-modulated martensite in epitaxial Ni-Mn-Ga films by co-sputtering, Acta Mater. 59 (2011) 75–81.

[21] R. Niemann, A. Backen, S. Kauffmann-Weiss, C. Behler, U.K. Rössler, H. Seiner, O. Heczko, K. Nielsch, L. Schultz, S. Fähler, Nucleation and growth of hierarchical martensite in epitaxial shape memory films, Acta Mater. 132 (2017) 327–334.

[22] A. Diestel, V. Neu, A. Backen, L. Schultz, S. Fähler, Magnetic domain pattern in hierarchically twinned epitaxial Ni-Mn-Ga films, J. Phys.: Condens. Matter 25 (2013) 266002.

[23] M. Campanini, L. Nasi, S. Fabbrici, F. Casoli, F. Celegato, G. Barrera, V. Chiesi, E. Bedogni, C. Magén, V. Grillo, G. Bertoni, L. Righi, P. Tiberto, F. Albertini, Magnetic shape memory turns to nano: microstructure controlled actuation of free-standing nanodisks, Small 14 (2018) 1803027.

[24] M Kohl, M. Schmitt, A. Backen, L. Schultz, B. Krevet, S. Fähler, Ni-Mn-Ga shape memory nanoactuation, Appl. Phys. Lett. 104 (2014) 043111.

[25] C.S. Watson, C. Hollar, K. Anderson, W.B. Knowlton, P. Müllner, Magnetomechanical four-state memory, Adv. Funct. Mater. 23 (2013) 3995–4001.

[26] P.H. Davis, C.M. Efaw, L.K. Patten, C. Hollar, C.S. Watson, W.B. Knowlton, P. Müllner, Localized deformation in Ni-Mn-Ga single crystals, J. Appl. Phys. 123 (2018) 215102.

[27] R. Mansell, T. Vemulkar, D.C. Petit, Y. Cheng, J. Murphy, M.S. Lesniak, R.P. Cowburn, Magnetic particles with perpendicular anisotropy for mechanical cancer cell destruction, Sci. Rep. 7 (2017) 4257.

[28] C.A. Jenkins, R. Ramesh, M. Huth, T. Eichhorn, P. Pörsch, H.J. Elmers, G. Jakob, Growth and magnetic control of twinning structure in thin films of Heusler shape memory compound Ni_2MnGa, Appl. Phys. Lett. 93 (2008) 234101.

[29] T. Eichhorn, R. Hausmanns, G. Jakob, Microstructure of freestanding single-crystalline Ni_2MnGa thin films, Acta Mater. 59 (2011) 5067–5073.

[30] R. Niemann, S. Hahn, A. Diestel, A. Backen, L. Schultz, K. Nielsch, M.X. Wagner, S. Fähler, Reducing the nucleation barrier in magnetocaloric Heusler alloys by nanoindentation, APL Mater. 4 (2016) 064101.

[31] D.E. Newbury, D.C. Joy, P. Echlin, C.E. Fiori, J.I. Goldstein, Advanced Scanning Electron Microscopy and X-ray Microanalysis, Springer, Boston, MA, 1986, pp. 87–142.

[32] N. Matsunami, Y. Yamamura, Y. Itikawa, N. Itoh, Y. Kazumata, S. Miyagawa, S. Morita, K. Shimizu, H. Tawara, Energy dependence of the ion-induced sputtering yields of monatomic solids, At. Data Nucl. Data Tables 31 (1984) 1–80.

[33] R. Chulist, P. Czaja, T. Tokarski, I. Kuksgauzen, Y.I. Chumlyakov, Orthogonal shear process in Ni-Mn-Sn single crystal, Int. J. Plasticity 114 (2019) 63–71.

[34] B. Yang, T. Liu, X.W. Hao, Z.B. Li, Y.D. Zhang, G.W. Qin, M. Philippe, C. Esling, X. Zhao, L. Zuo, Crystallography of martensitic transformation in epitaxial $Ni_{50}Mn_{30}Ga_{20}$ thin film, Adv. Eng. Mater. 20 (2018) 1700171.

[35] A.G. Khachaturyan, Theory of Structural Transformations in Solids, Wiley, New York, USA, 1983.

[36] M. Trassinelli, M. Marangolo, M. Eddrief, V.H. Etgens, V. Gafton, S. Hidki, E. Lacaze, E. Lamour, C. Prigent, J.P. Rozet, S. Steydli, Y. Zheng, D. Vernhet, Suppression of the thermal hysteresis in magnetocaloric MnAs thin film by highly charged ion bombardment, Appl. Phys. Lett. 104 (2014) 081906.

[37] N. Zhou, C. Shen, M.X. Wagner, G. Eggeler, M.J. Mills, Y. Wang, Effect of Ni_4Ti_3 precipitation on martensitic transformation in Ti-Ni, Acta Mater 58 (2010) 6685–6694.

[38] A. Sharma, S. Mohan, S. Suwas, New insights into microstructural evolution of epitaxial Ni-Mn-Ga films on MgO (1 0 0) substrate by high-resolution X-ray diffraction and orientation imaging investigations, Philos. Mag. 98 (2018) 819–847.

[39] P. Machain, A.M. Condó, P. Domenichini, G. Pozo López, M. Sirena, V.F. Correa, N. Haberkorn, Martensitic transformation in as-grown and annealed near-stoichiometric epitaxial Ni_2MnGa thin films, Philos. Mag. 95 (2015) 2527–2538.

[40] J. Amodeo, S. Merkel, C. Tromas, P. Carrez, S. Korte-Kerzel, P. Cordier, J. Chevalier, Dislocations and plastic deformation in MgO crystals: a review, Crystals 8 (2018) 240–293.

[41] J. Amodeo, P. Carrez, B. Devincre, P. Cordier, Multiscale modelling of MgO plasticity, Acta Mater. 59 (2011) 2291–2301.